In situ detector calibration at CLIC.

D. Arominski [*†], J-J. Blaising [‡], D. Dannheim [*], A. Sailer [*]

On behalf of the CLICdp Collaboration

[*] *CERN, Switzerland,* [†] *Warsaw University of Technology, Poland,* [‡] *Laboratoire d'Annecy-le-Vieux de Physique des Particules, Annecy-le-Vieux, France*

Abstract

The Compact LInear Collider (CLIC) is proposed to run according to a staging scenario with centre-of-mass energies increasing from $\sqrt{s} = 380$ GeV to 3 TeV. Achieving good physics performance requires accurate alignment and calibration of the detector as well as regular monitoring of the alignment and calibration parameters. During physics runs this is achieved using particles from $ee, e\gamma$ and $\gamma\gamma$ interactions. Standard Model cross sections depend on the centre-of-mass energy. As a result, processes relevant for calibration are different at the different energies. This note discusses the main detector calibration topics at two different centre-of-mass energies of CLIC, $\sqrt{s} = 380$-350 GeV and 1.5 TeV. It estimates the total and differential muon rates available for the detector alignment as well as the performance reachable for the momentum scale and total energy scale calibration. For the first stage of CLIC, special calibration runs at $\sqrt{s} = 91.2$ GeV are also considered. After the first year of running the high muon rate allows an accurate alignment and a regular control of the alignment parameters. $Z \rightarrow \mu^+\mu^-$ and $K_S \rightarrow \pi^+ + \pi^-$ events allow a good control of the momentum resolution and an accurate determination of the global and differential momentum scale. At $\sqrt{s} = 91.2$ GeV the di-muon event sample provides a direct measurement of the momentum resolution and an accurate determination of the momentum scale. The di-jet event sample allows for a direct measurement of the di-jet energy resolution and a good determination of the di-jet energy scale. It allows also for the measurement of the flavour tagging efficiency. At the lowest centre-of-mass energy a measurement of the top mass will be done measuring the top production cross section in the energy range $\sqrt{s} = 340$ GeV to 350 GeV. This note presents also the method to measure the absolute centre-of-mass energy and the accuracy reachable for the top threshold scan.

This work was carried out in the framework of the CLICdp Collaboration

1 Introduction

The Compact Linear Collider (CLIC) [1], [2] is proposed to run according to a staging scenario with different centre-of-mass energies. For this study a scenario with stages at $\sqrt{s}$ = 380-350 GeV, 1.5 TeV and 3 TeV is assumed. Reaching good physics performance at each centre-of-mass energy requires accurate alignment and calibration of the detector as well as regular monitoring of the alignment and calibration parameters. The main calibration issues to address are:

- Muon and tracker system alignment;

- Detection and particle identification efficiency;

- Charged particle momentum resolution and momentum scale calibration;

- Calibration of the electromagnetic and hadronic calorimeters (ECAL and HCAL);

- Jet energy resolution and scale calibration;

- Missing transverse energy resolution and scale calibration;

- Flavour tagging performance.

Prior to the detector assembly, single and combined detector calibration will be performed in beam tests. Accurate detector alignment can only be done after the detector assembly. After alignment, the charged particle momentum resolution can be measured and compared with the resolution of Monte Carlo events; the absolute momentum scale can be determined using the invariant mass of well-known particles, e.g. M_Z and $M_{K_s^0}$. Once the momentum scale is known, the ECAL and HCAL calibration can be done using electrons and isolated charged hadrons by comparing the energy deposition in the calorimeters with the track momentum. Once the ECAL and HCAL calibration parameters are set, the energy resolution can be measured and the total energy scale can be determined using di-jet events originating from Z or W bosons.

The main contributions to the di-jet energy resolution are:

- Tracking efficiency;

- Momentum resolution;

- Calorimeter energy resolution;

- Leakage;

- Particle confusion;

- Jet confusion.

These contributions change with the centre-of-mass energy. At each energy, a comparison of data and Monte Carlo simulation for distributions related to the properties of the reconstructed hadronic final state will be performed. The di-jet invariant mass will be used to determine the di-jet energy resolution and the energy scale. At the lowest centre-of-mass energy, a measurement of the top mass will be done measuring the top production cross section in the energy range $\sqrt{s}$ = 340 GeV to 350 GeV. This note describes also the method to measure the absolute centre-of-mass energy and the centre-of-mass energy accuracy reachable for the top threshold scan.

2 Luminosities at CLIC

Table 1 lists the expected nominal luminosities at CLIC at the three centre-of-mass energies. At each centre-of-mass energy, the luminosity yield is reduced during the first three years. At $\sqrt{s} = 380$ GeV the scaling factor is 10%, 30% and 60% for year-1, year-2 and year-3 respectively [2]. For the subsequent energy stages, 1.5 TeV and 3 TeV, the accelerator is expected to reach its nominal performance after two years, and a ramp-up of 25% and 75% of the nominal luminosity in the first two years is assumed. The table shows also the expected luminosity at $\sqrt{s} = 91.2$ GeV. At the Z boson mass energy, assuming the nominal 380 GeV accelerator design, the luminosity is reduced by a factor 64 [3]. Table 1 shows also the expected luminosities per day in the first two years assuming a running efficiency of 75%.

Table 1: Expected luminosities at CLIC

$\sqrt{s}$ GeV	Luminosity [cm^{-2}s^{-1}]	Luminosity [cm^{-2}s^{-1}] Year-1	Luminosity/day [pb^{-1}]	Luminosity/day [pb^{-1}] Year-1	Luminosity/day [pb^{-1}] Year-2
380	1.5×10^{34}	1.5×10^{33}	970	97	290
1500	3.7×10^{34}	9.2×10^{33}	2400	600	1800
3000	5.9×10^{34}	1.5×10^{33}	3820	950	2850
91.2	2.3×10^{32}	2.3×10^{31}	15	1.5	4.5

At LEP1, the peak luminosity was $L_0 = 3.4 \times 10^{30}$cm^{-2}s^{-1}. Table 2 shows the LEP luminosities in 1994 and 1995 [4]. At CLIC at $\sqrt{s} = 91.2$ GeV despite a reduction of the luminosity the integrated

Table 2: LEP luminosities in 1994 and 1995.

Year	Beam energy [GeV]	Total Luminosity [pb^{-1}]	Average Luminosity [pb^{-1}/day]
1994	45.6	64	0.31
1995	45.6 - 70.0	47	0.23

luminosity per day will be significant larger than at LEP; it is therefore worthwhile to study the calibration potential at $\sqrt{s} = 91.2$ GeV.

3 Fast Event Simulation

The WHIZARD v2 program [5] was used to compute the cross sections and generate the events of the various processes considered for the detector calibration. The luminosity spectrum is generated using GUINEAPIG [6]; it is interfaced to WHIZARD using Circe2 [5]. The effects of Initial State Radiation (ISR) are also included in WHIZARD. Quark fragmentation and hadronisation is performed using the PYTHIA v6 program [7]. For the leptons, the default PYTHIA treatment of Final State Radiation (FSR) is used. At $\sqrt{s} = 91.2$ GeV, no luminosity spectrum has been generated, only ISR contributes to the luminosity spectrum. To take into account the detector resolution, the momentum and energy of the particles are randomly modified using Gaussian resolution parameters according to the particle type. For charged particles the momentum resolution function is:

$$\frac{\sigma(P)}{P} \approx a \cdot P \oplus b \cdot \frac{1}{\sqrt{\sin\theta}} \oplus c \cdot \frac{\cos\theta}{\sin\theta} \tag{1}$$

the parameter a, b and c represents the contribution from the curvature measurement, from the multiple-scattering and from the angular resolution respectively. The values were obtained by fitting the P_T res-

olution of full simulation data as a function of P_T [1]. For $\theta = 90°$ $a = 2.0 \times 10^{-5}$, $b = 2.0 \times 10^{-3}$ and $c = 2.0 \times 10^{-4}$. For tracks measured in the tracker barrel $\theta > 40°$ and $\theta < 140°$ parameter a is independent of θ. For tracks measured in the end cap disks the path length L depends on θ and therefore a depends on θ

$$a_\theta = a \times \left(\frac{\tan \theta_{40}}{\tan \theta} \right)^2 \tag{2}$$

For photons the energy resolution function is:

$$\frac{\sigma(E)}{E} = 0.15/\sqrt{E} \; [\text{GeV}] \tag{3}$$

For neutral hadrons the energy resolution function is:

$$\frac{\sigma(E)}{E} = 0.55/\sqrt{E} \; [\text{GeV}] \tag{4}$$

In the introduction, the main contributions to the total energy resolution are listed. Several of them cannot be approximated in a fast simulation; e.g. leakage, particle confusion. This leads to an underestimation of the total energy resolution. To make the fast simulation more realistic the following assumptions have been included:

- track efficiency 99%;

- No charged particle identification; mass of charged hadron = pion mass;

- No neutral particle identification; mass of neutral hadron = kaon mass.

The Fastjet exclusive *kt* algorithm [8] is used for jet clustering.

4 Fractional Luminosities

CLIC is not only an $e^+ e^-$ collider, it also collides photons and electrons (positrons) with photons. The instantaneous luminosity of these collisions are not the same and for a given time period the integrated luminosities are different. Table 3 shows the instantaneous luminosities normalized to the $e^+ e^-$ luminosity for different centre-of-mass energies. To estimate the particle production rates these luminosity correction factors [9] are taken into account.

Table 3: Luminosity correction factors

$\sqrt{s} =$		350 GeV	380 GeV	1500 GeV	3000 GeV
Interaction	Luminosity correction				
$e^+ e^-$		1	1	1	1
$e^- \gamma$	$L(e^- \gamma)/L(e^+ e^-)$	0.53	0.55	0.75	0.79
$e^+ \gamma$	$L(e^+ \gamma)/L(e^+ e^-)$	0.53	0.55	0.75	0.79
$\gamma \gamma$	$L(\gamma \gamma)/L(e^+ e^-)$	0.34	0.36	0.64	0.70

5 Detector Alignment and Calibration at $\sqrt{s}$ = 380 GeV

Table 4 shows the cross sections of the main muon final state processes at $\sqrt{s}$ = 380 GeV. The cross section calculation and event generation was done for muons with an energy larger than 5 GeV and a polar angle of the muon θ_μ between $10°$ and $170°$. The table shows also the number of events assuming an integrated luminosity of $1\,\text{fb}^{-1}$ and taking into account the luminosity factors. For an integrated luminosity of $1\,\text{fb}^{-1}$, the total number of events produced is about 5×10^5.

Table 4: Cross sections of $e^+ e^-$, $e^- \gamma$ and $\gamma \gamma$ interactions with muon final states at $\sqrt{s}$ = 380 GeV

Process	σ [fb] $E_\mu > 5\,\text{GeV}; 10° < \theta_\mu < 170°$	Luminosity factor	Events / fb^{-1}
$e^+ e^- \to \mu^+ + \mu^-\,(\gamma)$	2.0×10^3	1	2.0×10^3
$e^+ e^- \to e^- \bar{\nu}_e \mu^+ \nu_\mu\,(\times 2)$	1.0×10^5	1	2.0×10^5
$e^+ e^- \to e^+ e^- \mu^+ \mu^-$	3.0×10^4	1	3.0×10^4
$e^- \gamma \to \mu^+ \mu^- e^-\,(\times 2)$	2.8×10^5	0.55	1.3×10^5
$\gamma \gamma \to \mu^+ \mu^-$	6.4×10^5	0.36	1.5×10^5
All			4.7×10^5

Table 5 shows the cross sections for di-jet final state processes at $\sqrt{s}$ = 380 GeV. It shows also the number of hadronic final state events assuming an integrated luminosity of $1\,\text{fb}^{-1}$ and taking into account the luminosity factors.

Table 5: Cross sections of $e^+ e^-$, $e^- \gamma$ and $\gamma \gamma$ interactions with di-jet final states at $\sqrt{s}$ = 380 GeV

Process	σ [fb] $E_q > 10\,\text{GeV}; 10° < \theta_q < 170°$	Luminosity factor	Events / fb^{-1}
$e^+ e^- \to q \bar{q} \gamma$	1.7×10^4	1	1.7×10^4
$e^+ e^- \to q \bar{q} e^+ e^-$	1.8×10^3	1	1.8×10^3
$e^+ e^- \to e^- \bar{\nu}_e q \bar{q}\,(\times 2)$	1.2×10^3	1	1.2×10^3
$e^- \gamma \to \nu_e q \bar{q}\,(\times 2)$	1.1×10^3	0.45	5.0×10^2
$e^- \gamma \to e^- q \bar{q}\,(\times 2)$	8.0×10^4	0.45	3.6×10^4

5.1 Tracker Alignment

Tracking system alignment requires a large number of tracks. For example, the alignment of the CMS tracker for the first high-luminosity data-taking period during the year 2011 was done using tracks from several data sets: isolated muons originating from leptonic W decays, tracks from minimum bias events, muons from Z-boson decays and cosmic ray tracks. The total number of tracks was about 2×10^7 [10].

Figure 1(a) shows the muon momentum distribution of the processes listed in Table 4. The momentum of the muons extends over a large range and is adequate for the tracking systems alignment. Figure 1(b) shows the angular distribution of the muons. The plots show the distributions corresponding to an integrated luminosity of $1\,\text{fb}^{-1}$. The number of tracks in the central region is about 5×10^3 per bin of $1°$ in polar angle θ; it is significantly higher in the forward region. The muon rate is about 8×10^5 tracks per fb^{-1} providing a total rate of about 1.4×10^7 muon tracks at the end of the first year and 4.3×10^7 at the end of the second year.

(a) Muon momentum distribution
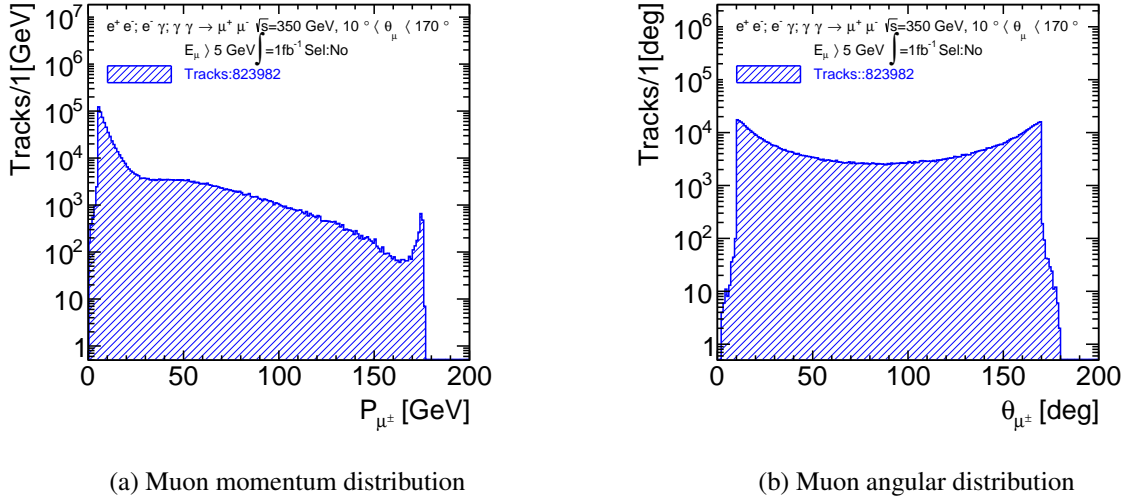

(b) Muon angular distribution

Figure 1: $e^+ e^-$, $e^- \gamma$ and $\gamma \gamma$ interactions with muon final states at $\sqrt{s}$ = 350 GeV (a) Muon momentum distribution (b) Muon angular distribution

5.2 Momentum Resolution and Momentum Scale Calibration

Figure 2(a) shows the di-muon mass vs the di-muon energy of the processes $e^+ e^- \rightarrow \mu^- \mu^+$ and $e^- \gamma \rightarrow \mu^- \mu^+ e^-$ at $\sqrt{s}$ = 350 GeV. The number of events in the plot correspond to an integrated luminosity of 5 fb^{-1}. The momentum of the muons was smeared using the charged particle momentum resolution given in section 3. Figure 2(b) shows the projection on the di-muon mass axis; the Z peak is clearly visible.

(a) Di-muon mass vs di-muon energy

(b) Di-muon invariant mass spectrum
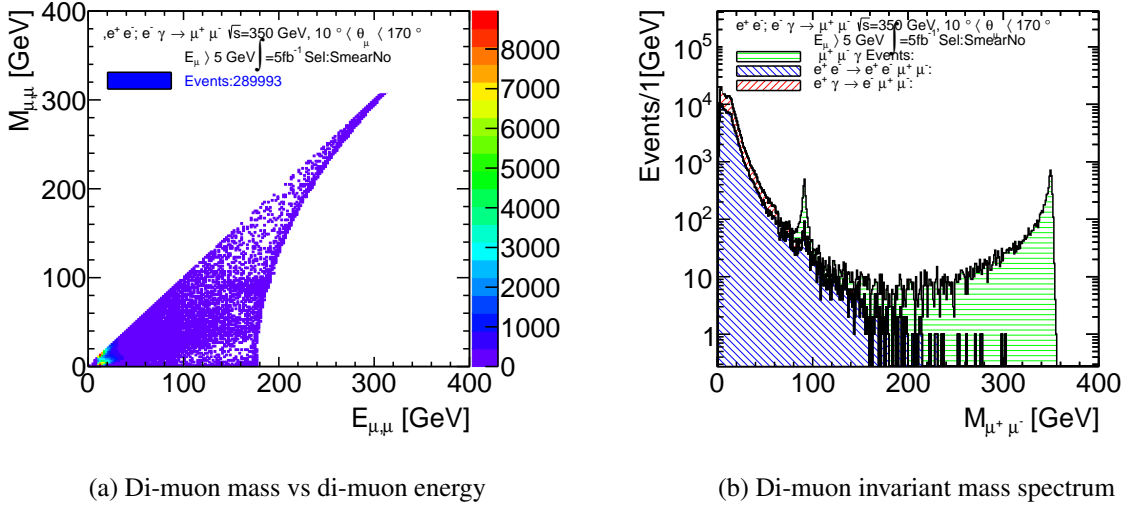
Figure 2: $e^+ e^- \rightarrow \mu^- \mu^+$ and $e^- \gamma \rightarrow \mu^- \mu^+ e^-$ at $\sqrt{s}$ = 350 GeV with momentum smearing (a) Di-muon mass vs di-muon energy (b) Di-muon invariant mass spectrum

Figure 3(a) shows the muon invariant mass of the processes $e^+ e^- \rightarrow \mu^- \mu^+$ and $e^- \gamma \rightarrow \mu^- \mu^+ e^-$ at $\sqrt{s}$ = 350 GeV after a cut requiring that the di-muon energy is greater than 160 GeV. The $e^- \gamma \rightarrow \mu^- \mu^+ e^-$ background is strongly reduced. Figure 3(b) shows the fit of the muon invariant mass in the Z region. M_Z = 91.16 ± 0.05 GeV and $\Gamma(M_Z)$ = 2.86 ± 0.13 GeV. With an integrated luminosity of 5 fb^{-1} the

global momentum scale can be determined with a relative uncertainty $\sigma(M_Z)/M_Z = 5 \times 10^{-4}$. With more luminosity, the momentum scale as a function of the angle can be determined.
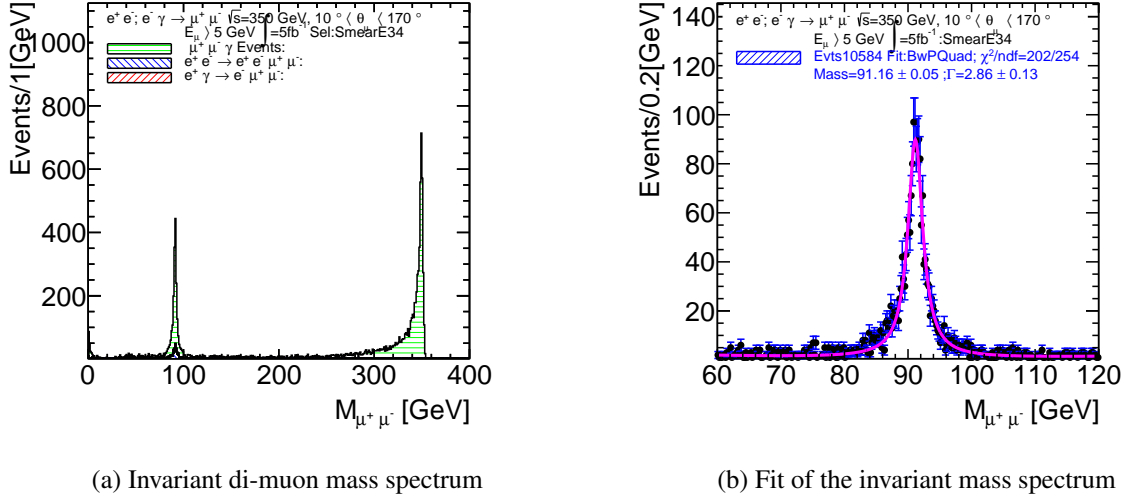

(a) Invariant di-muon mass spectrum

(b) Fit of the invariant mass spectrum

Figure 3: $e^+ e^- \to \mu^- \mu^+$ and $e^- \gamma \to \mu^- \mu^+ e^-$ at $\sqrt{s} = 350$ GeV after di-muon energy cut (a) Invariant di-muon mass spectrum (b) Fit of the invariant mass spectrum

The charged particle momentum scale can also be determined measuring the $\pi^+ \pi^-$ invariant mass of $K_S^0 \to \pi^+ \pi^-$ events. K_S^0 particles are produced in $\pi^+ \pi^- \to \tau^+ \tau^-$ interactions and in all processes with hadronic final states. The following plots illustrate the potential of momentum scale measurement using K_S^0 decays in hadronic events. Figure 4(a) shows the hadron momentum distribution of the charged hadrons in the process $e^+ e^-$ and $e^- \gamma \to q \bar{q}$. Figure 4(b) shows the fit of the $\pi^+ \pi^-$ invariant mass in the K_S^0 mass region. The number of events in the plots correspond to an integrated luminosity of $1\ \text{fb}^{-1}$, $M_{K_s^0} = 0.4976 \pm 2 \times 10^{-5}$ GeV. With an integrated luminosity of $1\ \text{fb}^{-1}$ the global momentum scale can be determined with a relative uncertainty $\delta(M_{K_s^0})/M_{K_s^0} = 4 \times 10^{-5}$.

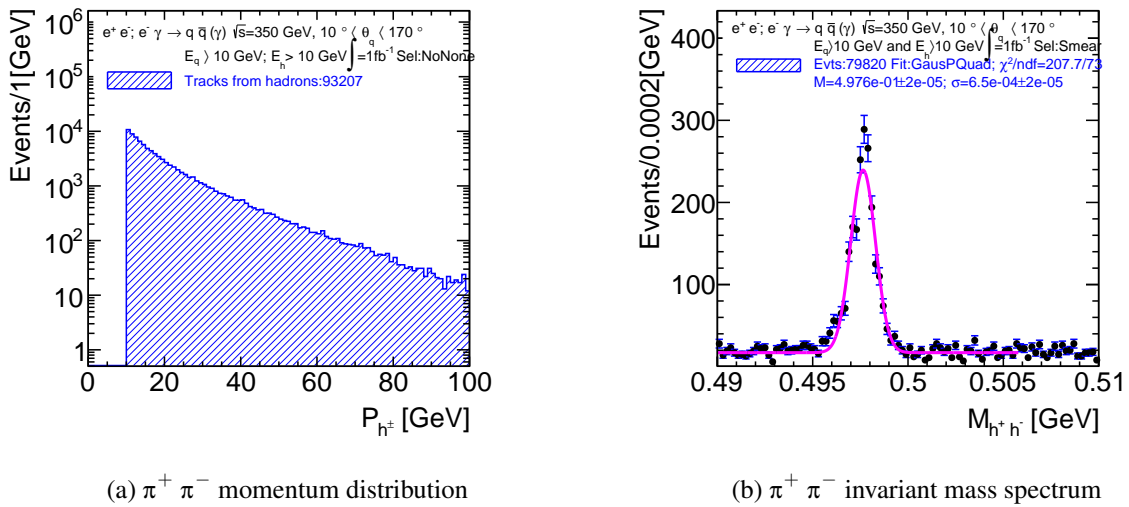(a) $\pi^+ \pi^-$ momentum distribution

(b) $\pi^+ \pi^-$ invariant mass spectrum

Figure 4: $e^+ e^-$ and $e^- \gamma \to q \bar{q}\ (\gamma)$ at $\sqrt{s} = 350$ GeV (a) $\pi^+ \pi^-$ momentum distribution (b) $\pi^+ \pi^-$ invariant mass spectrum

At $\sqrt{s} = 380$ GeV, $Z \rightarrow \mu^+\,\mu^-$ and $K_S^0 \rightarrow \pi^+\,\pi^-$ events allow a good control of the momentum resolution and an accurate determination of the global and differential momentum scale.

5.3 Di-jet Energy Resolution and Energy Scale

Figure 5(a) shows the di-jet invariant mass vs the di-jet energy after quark fragmentation and hadronisation and with particle energy smearing for the processes $e^+\,e^-$ and $e^-\,\gamma \rightarrow q\,\overline{q}\,(\gamma)$ at $\sqrt{s} = 350$ GeV. The Fastjet exclusive *kt* algorithm is used for jet clustering, the number of required jets is two and the jet radius parameter R is 1.0. Figure 5(b) shows the projection on the mass axis for the different processes.
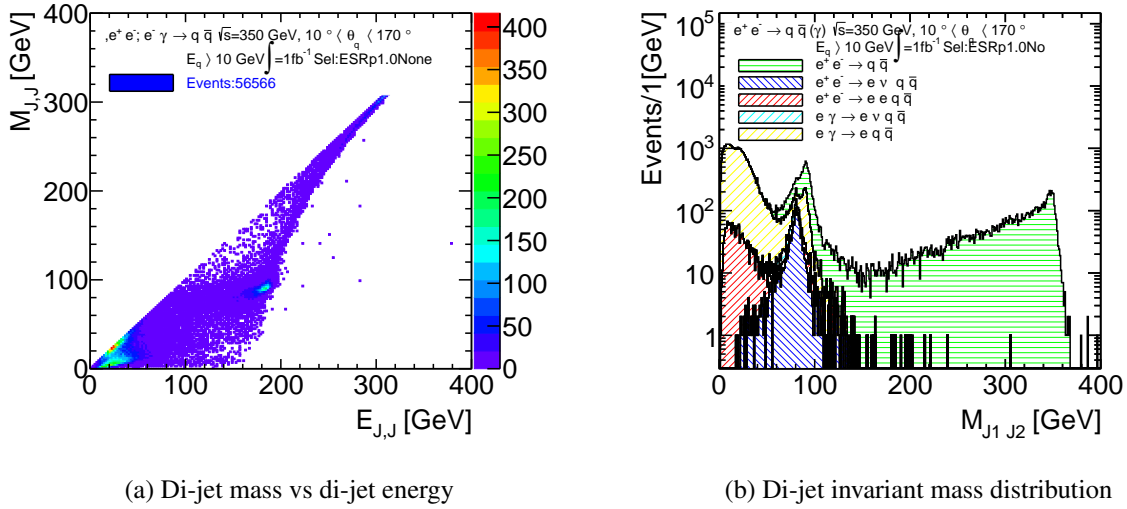
(a) Di-jet mass vs di-jet energy

(b) Di-jet invariant mass distribution

Figure 5: $e^+\,e^-$ and $e^-\,\gamma \rightarrow q\,\overline{q}\,(\gamma)$ at $\sqrt{s} = 350$ GeV. (a) Di-jet mass vs di-jet energy (b) Di-jet invariant mass distribution

Figure 6(a) shows the di-jet invariant mass of the processes $e^+\,e^-$ and $e^-\,\gamma \rightarrow q\,\overline{q}\,(\gamma)$ after a cut requiring the di-jet energy to be greater than 130 GeV. The $e^-\,\gamma \rightarrow q\,\overline{q}$ background is strongly reduced. Figure 6(b) shows the fit of di-jet invariant mass in the Z region. The fit function is a Breit-Wigner function for the peak and a quadratic function for the background. The fit result is $M_Z = 90.43 \pm 0.07$ GeV and $\Gamma_Z = 9.98$ GeV. At $\sqrt{s} = 350$ GeV, $Z \rightarrow q\,\overline{q}$ events allow for a good control of the di-jet energy resolution and an accurate determination of the global and differential di-jet energy scale. It allows also for the measurement of the heavy flavour tagging efficiency. Heavy flavour tagging efficiency measurement can also be done using the process $e^+\,e^- \rightarrow ZZ \rightarrow l^+\,l^-\,q\,\overline{q}$. The event selection requires di-muon or di-electron events compatible with the Z mass; it is only after the second year that the event rate is large enough to use this process to measure the heavy flavour tagging efficiency.

5.4 Absolute Centre-of-mass Energy Determination

At the lowest centre-of-mass energy, a measurement of the top mass will be done measuring the top production cross section for ten different centre-of-mass values in the energy range from $\sqrt{s} = 340$ GeV to 350 GeV. An integrated luminosity of $10\,\mathrm{fb}^{-1}$ will be used for each cross section measurement. The statistical accuracy of top mass measurement is 27 MeV for the nominal luminosity spectrum. To estimate the systematic error it is necessary to know the accuracy on the centre-of-mass energy. The measurement of the centre-of-mass energy can be done using $e^+\,e^- \rightarrow \mu^+\,\mu^-\,(\gamma)$ events. In absence of initial state radiation the centre-of-mass energy is $\sqrt{s} = E_{\mu^+} + E_{\mu^-}$. In presence of initial state radiation, the momentum of the photon can be inferred using the momentum of the di-muon system and $\sqrt{s}$ is
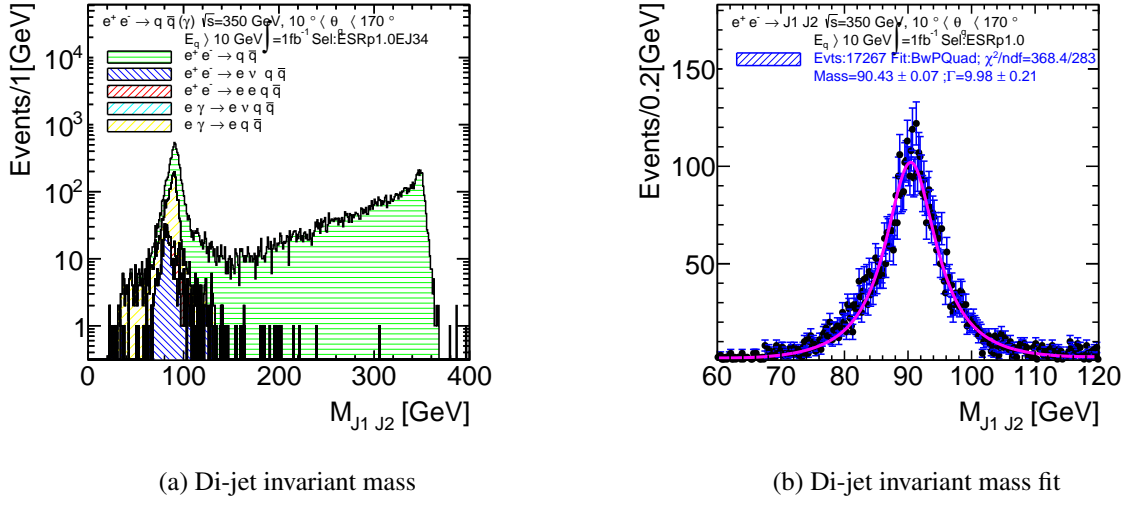
(a) Di-jet invariant mass

(b) Di-jet invariant mass fit

Figure 6: e^+ e^- and e^- $\gamma \to q$ $\bar{q}$ (γ) at $\sqrt{s} = 350$ GeV after di-jet energy cut. (a) Di-jet invariant mass (b) Di-jet invariant mass fit

determined using the following relation:

$$\sqrt{s} = E_{\mu^+} + E_{\mu^-} + |\vec{P}_{\mu^+} + \vec{P}_{\mu^-}| \tag{5}$$

Figure 7(a) shows the reconstructed $\sqrt{s}$ distribution obtained using formula 5. Figure 7(b) shows the di-muon invariant mass distribution. To reduce the e^+ e^- μ^+ μ^- and e^- μ^+ μ^- backgrounds ,which extend into the $\sqrt{s}$ peak distribution, a cut on the di-muon invariant mass is applied.
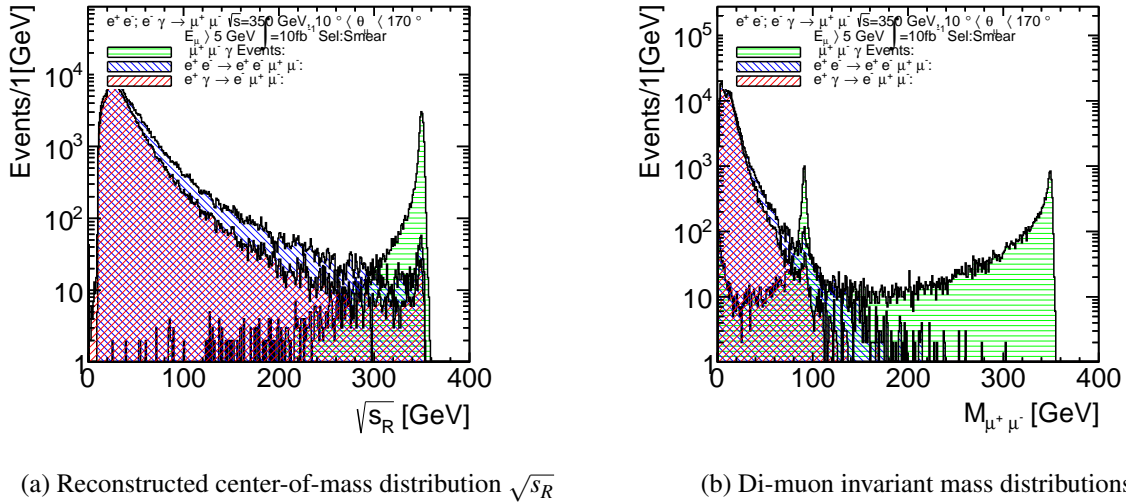
(a) Reconstructed center-of-mass distribution $\sqrt{s_R}$

(b) Di-muon invariant mass distributions

Figure 7: e^+ $e^- \to \mu^-$ μ^+ μ at $\sqrt{s} = 350$ GeV (a) Reconstructed center-of-mass distribution $\sqrt{s_R}$ (b) Di-muon invariant mass distributions

Figure 8(a) shows the reconstructed center-of-mass distribution $\sqrt{s_R}$ for events having a di-muon invariant mass greater than 300 GeV. The background is strongly suppressed. Figure 8(b) shows the fit of the reconstructed $\sqrt{s}$ distribution for events with a di-muon invariant mass greater than 300 GeV, $\sqrt{s} = 349.91 \pm 0.03$ GeV. At $\sqrt{s} = 350$ GeV, for an integrated luminosity of $100\,\mathrm{fb}^{-1}$, the centre-of-mass energy can be determined with an accuracy better than 10 MeV.

(a) Reconstructed center-of-mass distribution $\sqrt{s_R}$
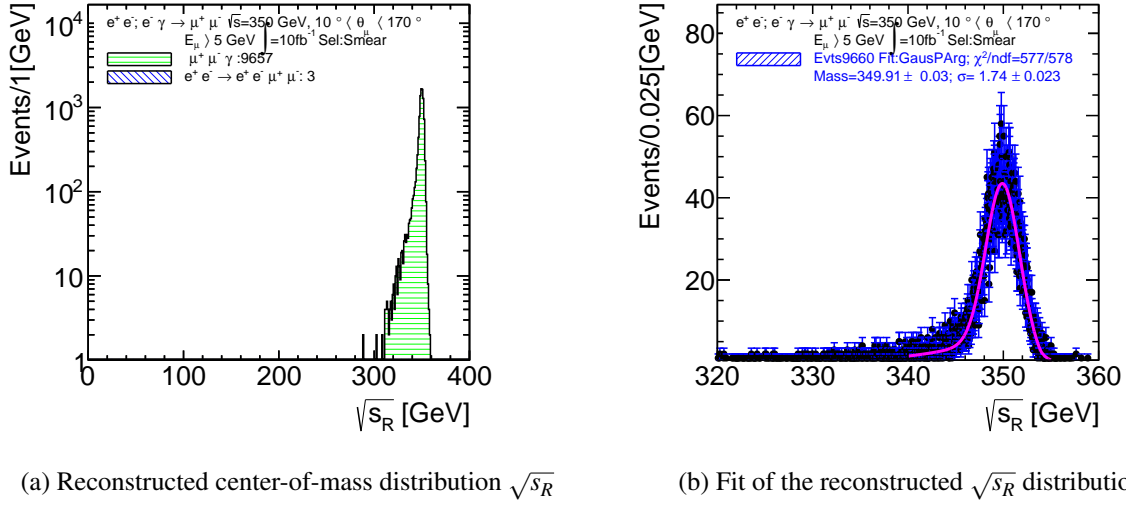
(b) Fit of the reconstructed $\sqrt{s_R}$ distributions

Figure 8: $e^+ e^- \to \mu^- \mu^+ \mu$ at $\sqrt{s}$ = 350 GeV (a) Reconstructed center-of-mass distribution $\sqrt{s_R}$ (b) Fit of the reconstructed $\sqrt{s_R}$ distributions

6 Detector Alignment and Calibration at $\sqrt{s}$=1500 GeV

Table 6 and Table 7 show the cross sections for muon final state and for di-jet final state processes respectively. They also show the expected number of events assuming an integrated luminosity of 1 fb^{-1} and taking into account the luminosity factors. In the first year, it will take about 6 days to reach an integrated luminosity of 1 fb^{-1}.

Table 6: Cross sections of $e^+ e^-$, $e^- \gamma$ and $\gamma\gamma$ interactions with muon final states at $\sqrt{s}$ = 1500 GeV.

Process	σ [fb]	Luminosity	Events / fb^{-1}
	$E_\mu > 5$ GeV; $10^\circ < \theta_\mu < 170^\circ$	factor	
$e^+ e^- \to \mu^+ + \mu^-$ (γ)	2.0×10^2	1	2.0×10^2
$e^+ e^- \to e^- \bar{\nu}_e \mu^+ \nu_\mu$ ($\times 2$)	6.5×10^5	1	6.5×10^5
$e^+ e^- \to e^+ e^- \mu^+ \mu^-$	3.8×10^4	1	3.8×10^4
$e^- \gamma \to \mu^+ \mu^- e^-$ ($\times 2$)	2.4×10^5	0.75	1.8×10^5
$\gamma \gamma \to \mu^+ \mu^-$	3.4×10^5	0.64	2.2×10^5
All			1.2×10^6

Table 7: Cross sections of $e^+ e^-$, $e^- \gamma$ and $\gamma \gamma$ interactions with di-jet final states at $\sqrt{s}$ = 1500 GeV.

Process	σ [fb]	Luminosity factor	Events / fb^{-1}
	$E_q > 10$ GeV; $10^\circ < \theta_q < 170^\circ$	factor	
$e^+ e^- \to q \bar{q} \gamma$	1.2×10^3	1	1.2×10^3
$e^+ e^- \to q \bar{q} e^+ e^-$	1.2×10^4	1	1.2×10^4
$e^+ e^- \to e^- \bar{\nu}_e q \bar{q}$ ($\times 2$)	4.4×10^3	1	4.4×10^3
$e^+ \gamma \to \nu_e q \bar{q}$ ($\times 2$)	2.5×10^4	0.75	1.9×10^4
$e^+ \gamma \to e^- q \bar{q}$ ($\times 2$)	8.7×10^4	0.75	6.5×10^4

6.1 Tracker Alignment

Figure 9(a) shows the momentum distribution of the muons of the processes listed in Table 6. The number of events corresponds to an integrated luminosity of $1\,\text{fb}^{-1}$. The total track rate is about 1.4×10^6 per fb^{-1}. The number of muons in the range of 50 to 100 GeV is about 1×10^4. Figure 9(b) shows the angular distribution of the muons. The number of tracks in the central region is about 8×10^3 per bin of 1° in polar angle θ; it is significantly higher in the forward region. The total number of muon tracks available at the end of the first year is about 1.5×10^8 and 4.5×10^8 at the end of the second year.

(a) Muon momentum distribution

(b) Muon angular distribution
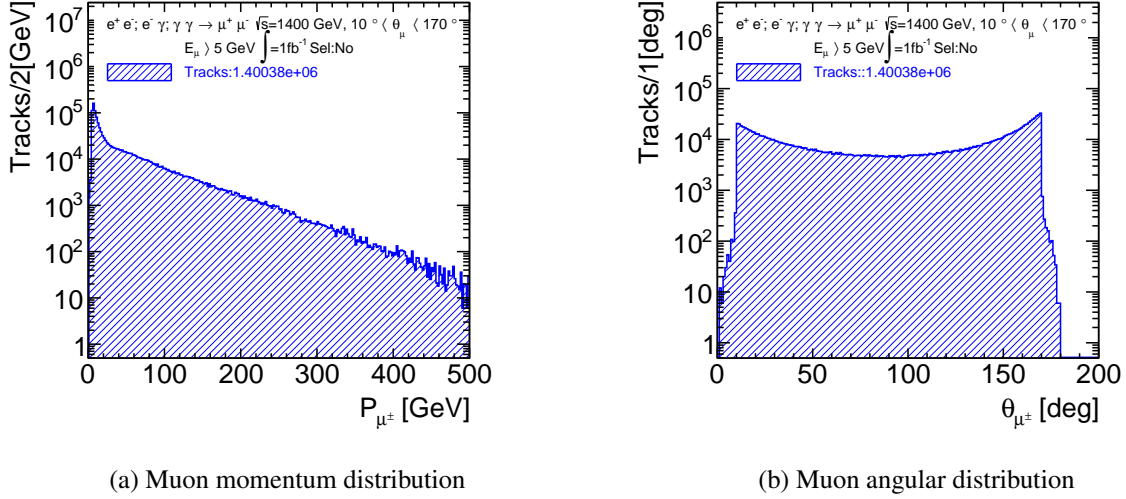
Figure 9: $e^+\,e^-$, $e^-\,\gamma$ and $\gamma\,\gamma$ interactions with muon final states at $\sqrt{s} = 1400\,\text{GeV}$ (a) Muon momentum distribution (b) Muon angular distribution

6.2 Momentum Resolution and Momentum Scale Calibration

At 1.5 TeV, the cross section of the process $e^+\,e^- \rightarrow \mu^+\,\mu^-\,\gamma$ is 200 fb and the fraction of events with return to the Z is only 5%. Therefore, the $Z \rightarrow \mu^+\,\mu^-$ yield is too small to allow a determination of the momentum scale using the di-muon mass. The measurement of the charged particle momentum scale is done measuring the $\pi^+\,\pi^-$ invariant mass of $K_S^0 \rightarrow \pi^+\,\pi^-$ events. Figure 10(a) shows the hadron momentum distribution of the charged hadrons in the processes $e^+\,e^-$ and $e^-\,\gamma \rightarrow q\,\bar{q}$. Figure 10(b) shows the fit of the $\pi^+\,\pi^-$ invariant mass in the K_S^0 mass region. The number of events in the plots correspond to an integrated luminosity of $1\,\text{fb}^{-1}$, $M_{K_s^0} = 0.4977 \pm 2 \times 10^{-5}$ GeV. With an integrated luminosity of $1\,\text{fb}^{-1}$ the relative uncertainty on the global momentum scale is $\delta(M_{K_s^0})/M_{K_s^0} = 4 \times 10^{-5}$. After the first year the high rate of K_S^0 allows an accurate determination of the momentum scale as a function of the polar angle.

6.3 Di-jet Energy Resolution and Energy Scale

Figure 11(a) shows the correlation between the di-quark invariant mass and the angle between the quarks for the processes $e^+\,e^-$ and $e^-\,\gamma \rightarrow q\,\bar{q}\,\gamma$ at $\sqrt{s} = 1400\,\text{GeV}$, the di-quark angle ranges from 10° to 170°. Figure 11(b) shows the di-quark invariant mass of the various processes, W events are clearly visible; a smaller Z peak is also visible. Figure 12(a) shows the di-jet invariant mass after quark fragmentation and hadronisation and without particle energy smearing; the Fastjet exclusive kt algorithm is used for jet clustering. The number of required jets is two and the jet radius parameter R is 1.0. The W-peak
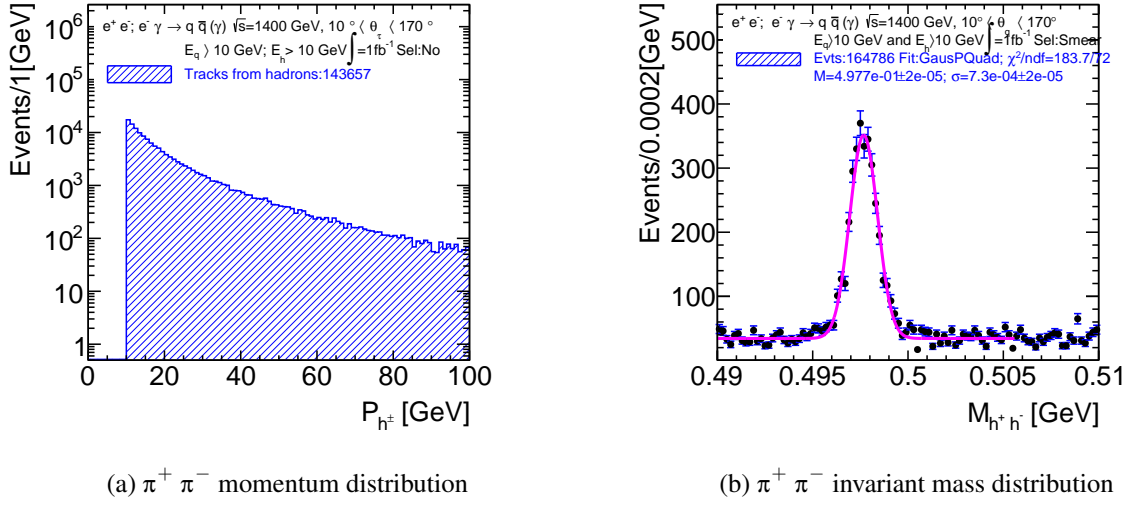
(a) $\pi^+ \pi^-$ momentum distribution

(b) $\pi^+ \pi^-$ invariant mass distribution

Figure 10: $e^+ e^-$ and $e^- \gamma \rightarrow q \bar{q} (\gamma)$ at $\sqrt{s}$ = 1400 GeV (a) $\pi^+ \pi^-$ momentum distribution (a) $\pi^+ \pi^-$ invariant mass distribution fit
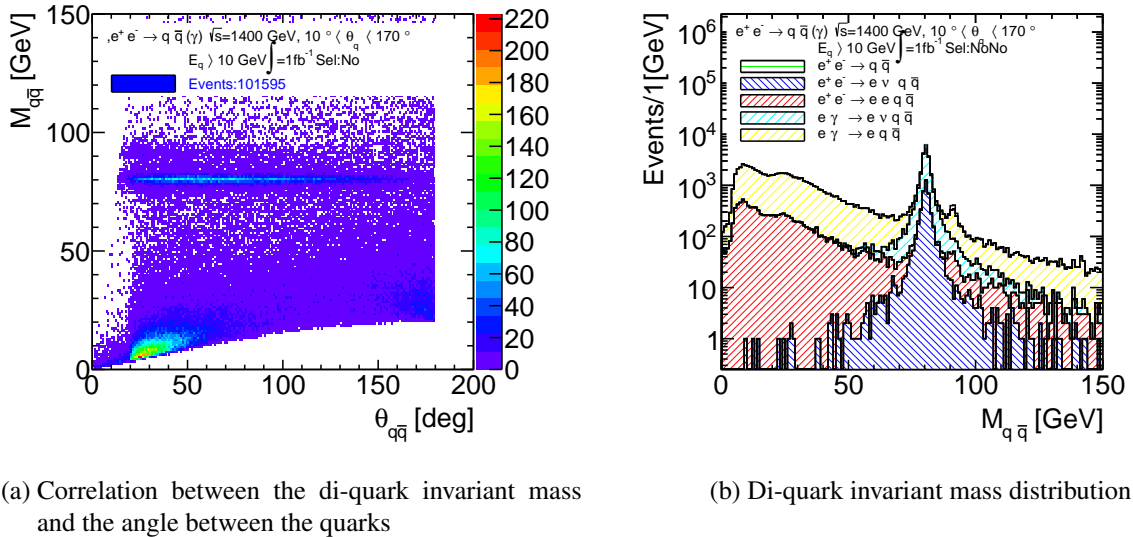

(a) Correlation between the di-quark invariant mass and the angle between the quarks

(b) Di-quark invariant mass distribution

Figure 11: $e^+ e^-$ and $e^- \gamma \rightarrow q \bar{q} \gamma$ at $\sqrt{s}$ = 1400 GeV (a) Correlation between the di-quark invariant mass and the angle between the quarks (b) Di-quark invariant mass distribution

width increase is due to the jet confusion created by the small angle between the jets. Figure 12(b) shows the di-jet invariant mass after quark fragmentation and hadronisation, and particle energy smearing. The W-peak width is only slightly increased by the energy resolution of the particles in the jet. Figure 13(a) shows the di-jet invariant mass fit in the W, Z region. The fit result is $M_W = 78.68 \pm 0.08$ GeV and $\Gamma_W = 10.05$ GeV. Figure 13(b) shows the di-jet invariant mass fit when rejecting events for which the $q\bar{q}$ pair comes from a Z. The fit result is $M_W = 78.58 \pm 0.07$ GeV and $\Gamma_W = 10.8$ GeV. The contribution of the Z $\rightarrow q \bar{q}$ events to the mass spectrum in the W region is small and does not bias significantly the W mass measurement.

At $\sqrt{s}$ = 1.5 TeV, the measurement of the W mass spectrum of $e^+ e^- \rightarrow e^- \bar{\nu}_e q \bar{q}$ and $e^+ \gamma \rightarrow \nu_e q \bar{q}$ events allows for an accurate determination of the di-jet energy scale. Heavy flavour tagging efficiency measurement can be done using the process $e^+ e^- \rightarrow ZZ \rightarrow 1^+ 1^- q \bar{q}$. The event selection
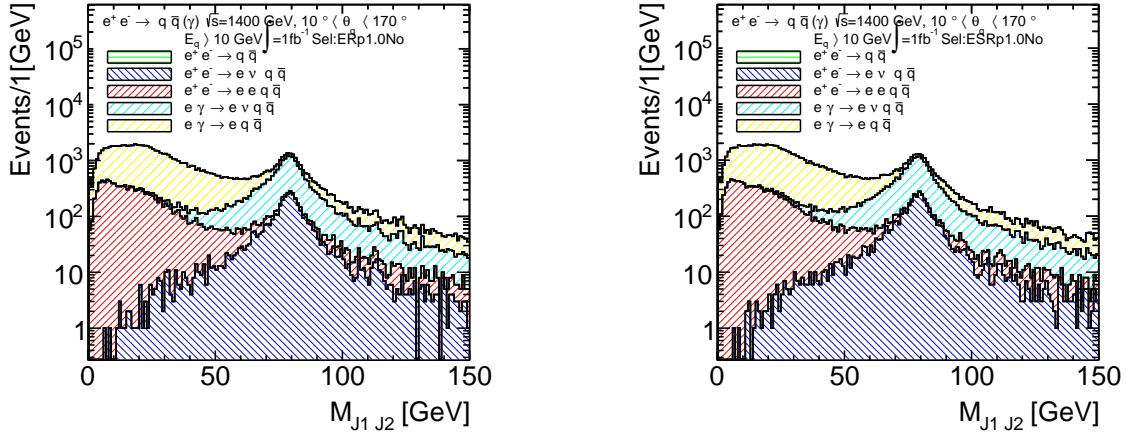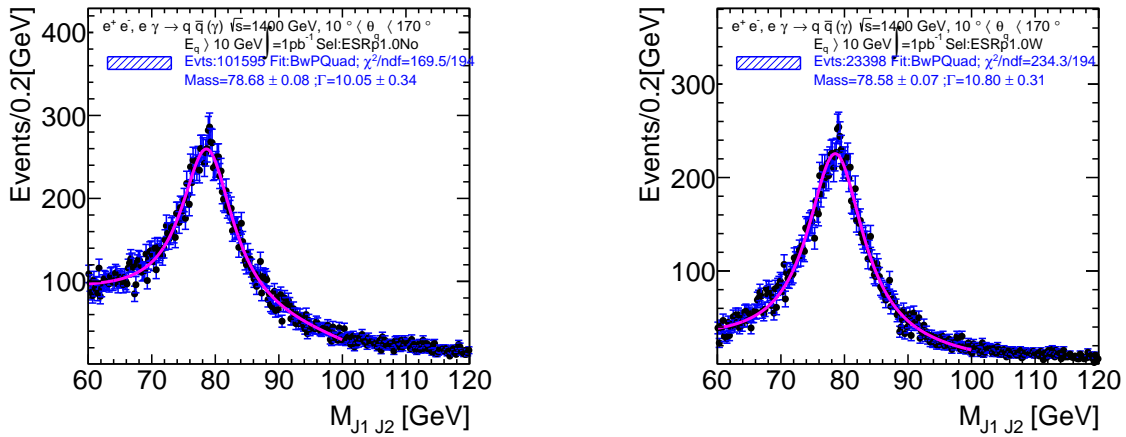
(a) Di-jet invariant mass spectrum after jet clustering and without particle smearing

(b) Di-jet invariant mass spectrum after jet clustering and particle smearing

Figure 12: $e^+ e^-$ and $e^- \gamma \to q \bar{q} \gamma$ at $\sqrt{s}$ = 1400 GeV (a) Di-jet invariant mass spectrum after jet clustering and without particle smearing (b) Di-jet invariant mass spectrum after jet clustering and with particle smearing

requires di-muon or di-electron events compatible with the Z mass. The cross section of the process $e^+ e^- \to l^+ l^- q \bar{q}$ is 16 fb. Figure 14(a) shows the di-muon invariant mass fit in the Z region. Figure 14(b) shows the di-jet invariant mass fit for $\mu^+ \mu^- q \bar{q}$ events with a di-muon mass between 80 GeV and 100 GeV. The data sample of the plots corresponds to an integrated luminosity of 600 fb^{-1}. At $\sqrt{s}$ = 1.5 TeV, $e^+ e^- \to l^+ l^- q \bar{q}$ events allow for a good control of the momentum scale, of the di-jet energy scale and of the heavy flavour tagging efficiency.

(a) Di-jet invariant mass spectrum; all events

(b) Di-jet invariant mass spectrum; no Z contribution

Figure 13: $e^+ e^-$ and $e^- \gamma \to q \bar{q} \gamma$ at $\sqrt{s}$ = 1400 GeV (a) Di-jet invariant mass spectrum fit; all events (b) Di-jet invariant mass spectrum fit; no Z contribution

(a) Di-muon invariant mass spectrum;
all events

(b) Di-jet invariant mass spectrum;
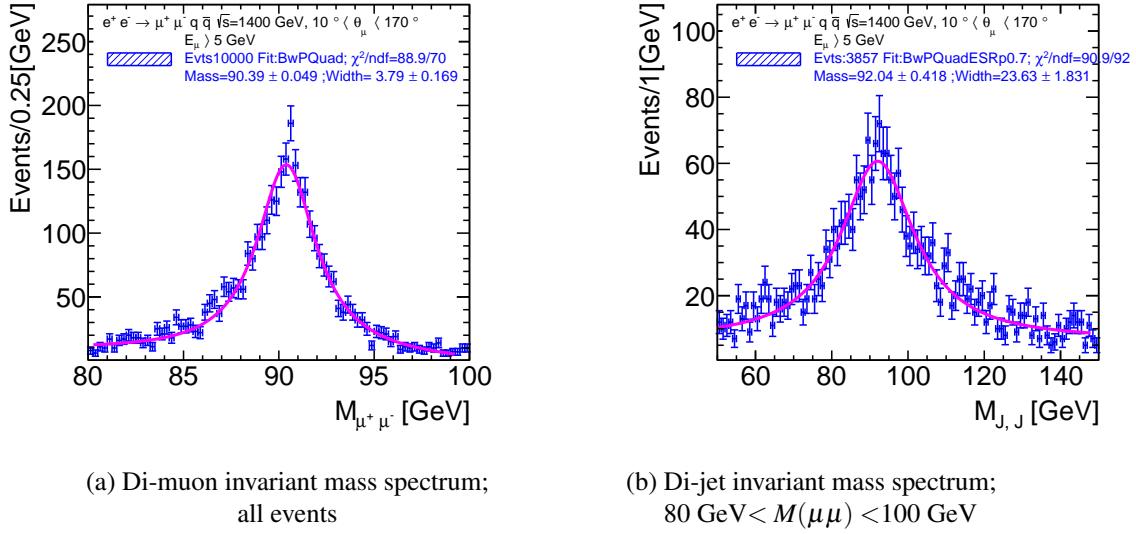80 GeV< $M(\mu\mu)$ <100 GeV

Figure 14: $e^+ e^- \rightarrow \mu^+ \mu^- q \bar{q}$ at $\sqrt{s}$ = 1400 GeV (a) Di-muon invariant mass spectrum; all events (b) Di-jet invariant mass spectrum for 80 GeV< $M(\mu\mu)$ <100 GeV

7 Detector Calibrations at $\sqrt{s}$ = 91.2 GeV

Table 8 shows the cross sections for $\mu^+ \mu^-$ and $q \bar{q}$ final states at $\sqrt{s}$ = 91.2 GeV; it also shows the event rates assuming an integrated luminosity of 1 pb^{-1}.

Table 8: Di-muon and di-jet final state cross sections and event rates at $\sqrt{s}$=91.2 GeV

Process	Cross section [fb]	Events / pb^{-1}
	$E_f > 10$ GeV and $10° < \theta_f < 170°$	
$e^+ e^- \rightarrow \mu^+ \mu^- \gamma$	1.47×10^6	1.5×10^3
$e^+ e^- \rightarrow q \bar{q} \gamma$	29.6×10^6	3×10^4

7.1 Momentum Resolution and Scale

Table 1 shows that in the first year of CLIC, at $\sqrt{s}$ = 91.2 GeV, the luminosity is 1.5 pb^{-1} per day. In the second year the expected luminosity is 4.5 pb^{-1} per day providing significant event samples for calibration. Figure 15(a) shows the muon momentum distribution (blue) of the process $e^+ e^- \rightarrow \mu^+ \mu^-$ after smearing. The figure also shows the fit result; $< P_\mu > = 45.56 \pm 0.006$ GeV and $\sigma(P) = 0.13$ GeV. For muons of 45 GeV the momentum resolution is dominated by the contribution of the multiple scattering; $\sigma(P)/P = 2.6 \times 10^{-3}$. The relative accuracy on the momentum scale is $\delta(P)/P = 7 \times 10^{-5}$. Figure 15(b) shows the $\mu^+ \mu^-$ invariant mass distribution (blue) as well as the fit result: $M_Z = 91.11 \pm 0.01$ GeV and $\sigma(M_Z) = 0.20 \pm 0.014$ GeV. At $\sqrt{s}$ = 91.2 GeV, there is little background and the di-muon event sample provides a direct measurement of the momentum resolution at 45.6 GeV as well as an accurate determination of the momentum scale with a minimum dependence on the Monte Carlo.

7.2 Di-jet Energy Resolution and Total Energy Scale

Figure 16(a) shows the di-jet total energy (blue) for events where the are two quarks in the barrel region. To avoid any bias the di-jet energy is measured without jet clustering. The red distribution shows the

(a) $\mu^+ \mu^-$ momentum distribution

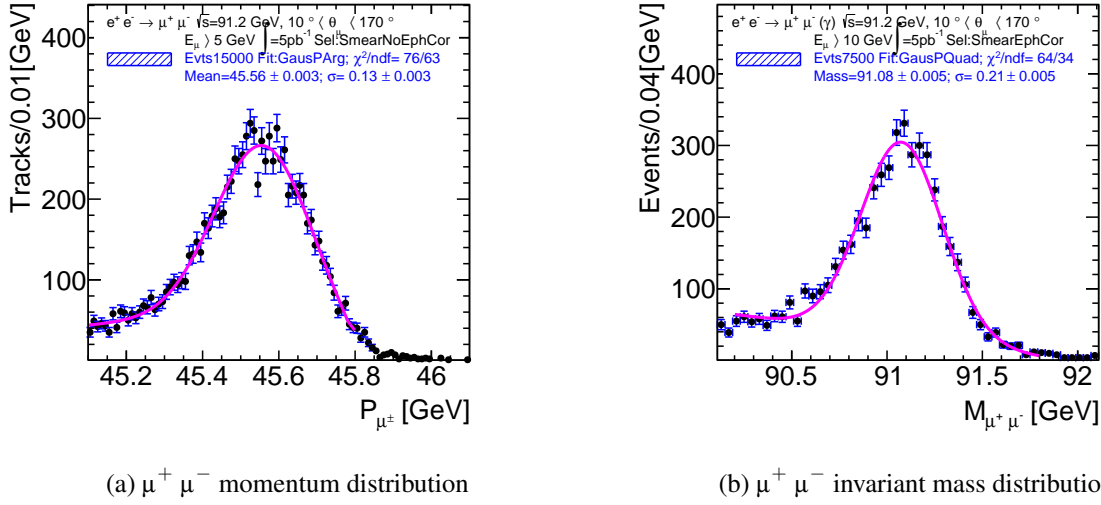(b) $\mu^+ \mu^-$ invariant mass distribution

Figure 15: $e^+ e^- \rightarrow \mu^+ \mu^-$ at $\sqrt{s} = 91.2$ GeV (a) $\mu^+ \mu^-$ momentum distribution (b) $\mu^+ \mu^-$ invariant mass distribution

true $\sqrt{s}$ distribution; the tail towards the low values is coming from events with ISR photons. The energy distribution is very narrow, in production mode one measures directly the di-jet energy resolution, there is no contribution from the natural Z width. The fit result is $< E_{tot} > = 90.57 \pm 0.016$ GeV and $\sigma(E_{tot}) = 1.52 \pm 0.03$ GeV. $\sigma(E_{tot})/E_{tot} = 1.7\%$, it leads to $\sigma(E_{Jet})/E_{Jet} = 2.4\%$.

Figure 16(b) shows the di-jet total energy for events where there are two quarks in the end-cap region. For this sample, there is an increase of the width of the energy distribution because some particles from the jets escape detection when the polar angle is below $7°$.

(a) Total energy distribution in barrel

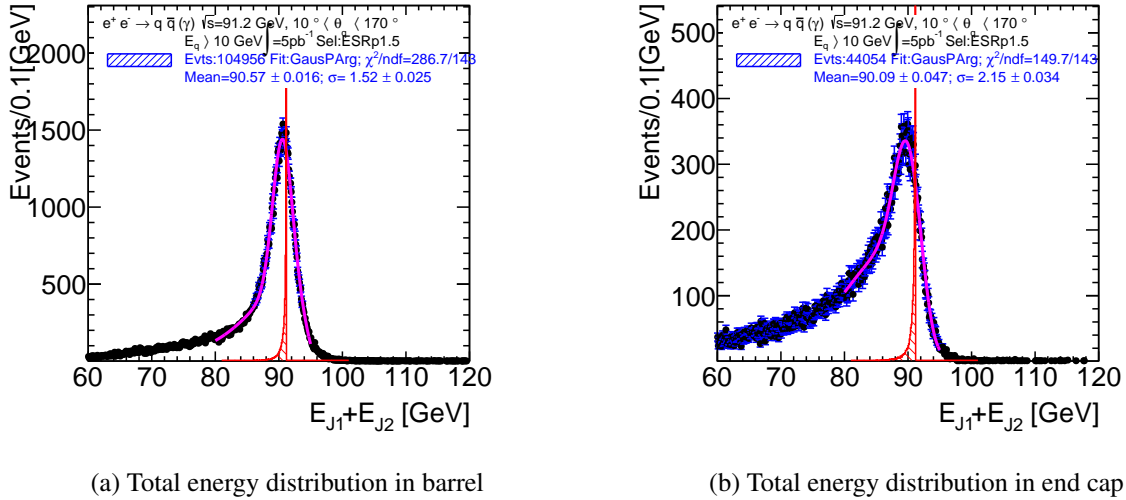(b) Total energy distribution in end cap

Figure 16: $e^+ e^- \rightarrow q \bar{q} \gamma$ at $\sqrt{s} = 91.2$ GeV (a) Total energy distribution in barrel (b) Total energy distribution in end cap

The di-jet event sample provides also a significant amount of data to measure the heavy flavour tagging efficiency.

8 Summary

At $\sqrt{s} = 380$ GeV and 1.5 TeV, the detector alignment can be done using $e^+ e^-$, $e^- \gamma$ and $\gamma \gamma$ interactions that have muon final states. At $\sqrt{s} = 380$ GeV, the total rate is about 1.4×10^8 muon tracks at the end of the first year. At $\sqrt{s} = 1500$ GeV, the total rate is about 1.5×10^8 muon tracks at the end of the first year. After the first year of running the high muon rate allows an accurate alignment and a regular control of the alignment parameters. At $\sqrt{s} = 380$ GeV, $Z \to \mu^+ \mu^-$ and $K_S^0 \to \pi^+ \pi^-$ events allow for an accurate control of the momentum resolution and an accurate determination of the global and differential momentum scale. $Z \to q \bar{q}$ events allow for a good control of the di-jet energy resolution and an accurate determination of the global and differential di-jet energy scale. It also allows the measurement of the heavy flavour tagging efficiency. At 1.5 TeV, the cross section of the process $e^+ e^- \to \mu^+ \mu^- \gamma$ is 200 fb and the fraction of events with a Z return is about 5%. As during the first year the integrated luminosity is only 0.6 fb^{-1} the $Z \to \mu^+ \mu^-$ yield does not allow for an accurate determination of the momentum scale using the di-muon mass. The measurement of the charged particle momentum scale is done measuring the $\pi^+ \pi^-$ invariant mass of $K_S^0 \to \pi^+ \pi^-$ events. At $\sqrt{s} = 1.5$ TeV, the measurement of the W mass spectrum of $e^+ e^- \to e^- \bar{\nu}_e q \bar{q}$ and $e^- \gamma \to \nu_e q \bar{q}$ events allows for an accurate determination of the di-jet energy scale. The contribution from $e^+ e^- \to e^+ e^- q \bar{q}$ and $e^- \gamma \to e^- q \bar{q}$ events does not bias the measurement of the di-jet energy scale. The process $e^+ e^- \to l^+ l^- q \bar{q}$. provides an additional data set allowing a control of the particle momentum scale of the di-jet energy scale and of the heavy flavour tagging efficiency. At $\sqrt{s} = 91.2$ GeV, there is little background. The di-muon event sample provides a direct measurement of the momentum resolution at 45.6 GeV and an accurate determination of the momentum scale. The di-jet event sample allows for a direct measurement of the di-jet energy resolution and an accurate determination of the di-jet energy scale. It also allows the flavour tagging efficiency measurement. The back-to-back event topology also allows for a detailed check of the detector hermicity. During the first stage of CLIC and after the first year, running at $\sqrt{s} = 91.2$ GeV provides unique calibration features and an excellent opportunity to optimize the detector performance.

9 Acknowledgments

References

[1] L. Linssen et al., eds., *CLIC Conceptual Design Report: Physics and Detectors at CLIC*, CERN-2012-003, CERN, 2012, arXiv: `1202.5940 [physics.ins-det]`.

[2] P. Burrows et al., eds., *The Compact Linear Collider (CLIC) 2018 Summary Report*, CERN-2018-005-M, CERN, 2018.

[3] D. Schulte, *Private Communication*, CERN.

[4] R. W. Assmann, *LEP Luminosity Revisited: Design and Reality*, proceedings of the Second Asian Particle Conference, Beijing, China, 2001.

[5] W. Kilian, T. Ohl, J. Reuter, *WHIZARD: Simulating Multi-Particle Processes at LHC and ILC*, Eur.Phys.J. **C71** (2011) 1742, DOI: `arXiv:0708.4233[hep-ph]`.

[6] D. Schulte, *Beam-beam simulations with GUINEA-PIG*, CERN-PS-99-014-LP, CERN, 1999.

[7] T. Sjostrand, S. Mrenna, P. Z. Skands, *PYTHIA 6.4 Physics and Manual*, JHEP **05** (2006),
DOI: `arXiv:hep-ph/0603175`.

[8] M. Cacciari, G. P. Salam, *Dispelling the N^3 myth for the k_t jet-finder*, Phys. Lett. **B641** (2006),
DOI: `arXiv:1111.6097`.

[9] D. Arominski et al., *CLIC Beam-beam interactions*, 2018,
DOI: `10.5281/zenodo.1467017`,
URL: `https://doi.org/10.5281/zenodo.1467017`.

[10] CMS Collaboration, *Alignment of the CMS tracker with LHC and cosmic ray data*,
Journal of Instrumentation (2014), DOI: `arXiv:1403.2286V2[physics-ins-det]`.